IOP Publishing Smart Materials and Structures
Smart Mater. Struct. 27 (2018) 044001 (16pp) https://doi.org/10.1088/1361-665X/aa94d6

Architectures for wrist-worn energy harvesting

R Rantz[1], M A Halim[1], T Xue[1], Q Zhang[2], L Gu[2], K Yang[2] and S Roundy[1]

[1] University of Utah, 1495 E 100 S (1550 MEK), Salt Lake City, UT 84112, United States of America
[2] Analog Devices, Inc., 804 Woburn St, Wilmington, MA 01887, United States of America

E-mail: robert.rantz@utah.edu

Received 6 May 2017, revised 28 September 2017
Accepted for publication 20 October 2017
Published 5 March 2018

Abstract

This paper reports the simulation-based analysis of six dynamical structures with respect to their wrist-worn vibration energy harvesting capability. This work approaches the problem of maximizing energy harvesting potential at the wrist by considering multiple mechanical substructures; rotational and linear motion-based architectures are examined. Mathematical models are developed and experimentally corroborated. An optimization routine is applied to the proposed architectures to maximize average power output and allow for comparison. The addition of a linear spring element to the structures has the potential to improve power output; for example, in the case of rotational structures, a 211% improvement in power output was estimated under real walking excitation. The analysis concludes that a sprung rotational harvester architecture outperforms a sprung linear architecture by 66% when real walking data is used as input to the simulations.

Keywords: energy harvesting, metaheuristic optimization, harvester architecture

(Some figures may appear in colour only in the online journal)

1. Introduction

The mechanical substructure of a wrist-worn vibration energy harvester responsible for the absorption of kinetic energy from its environment—herein referred to as the harvester *architecture*—distinct from the particular transduction mechanism which allows for the conversion of the absorbed kinetic energy from the mechanical domain to the electrical domain, is the focus of this work. The prevailing goal of an energy harvesting architecture is to maximize the amount of kinetic energy absorbed from the environment, per unit volume, as possible over a range of input excitations; numerous novel device architectures have been developed in order to achieve this purpose.

Rotational architectures are popular for body-worn energy harvester applications [1–9], perhaps motivated by some successful commercial products with rotational architectures [10, 11], the lack of displacement limitations, and a watch-like form factor. Other architectures in the literature specialize in responding to linear forcing along a particular direction by making use of a seismic mass given one degree of translational freedom [12–16]. Some related architectures allow for a seismic mass to move in more than one dimension, or may require a nonholonomic system description [17, 18].

In spite of the numerous device architectures explored in the literature, it remains unclear if one single architecture is inherently superior to another in its capacity to absorb kinetic energy from the wrist under a range of typical excitations. One major reason for this lack of clarity is inconsistency in device volumes among the devices explored in the literature; a large device is typically capable of producing more power than a smaller device. Although comparisons of power density may provide a potential remedy, variation in the transducer technologies employed by devices in the literature serve to confound a comparison of disparate architectures; the benefits bestowed upon a device by virtue of judicious selection of a particular transducer technology may belie the disadvantages of a suboptimal choice in mechanical substructure. Decoupling the effect of each is a major difficulty when the goal is to determine a mechanical device

architecture that is best suited for a particular application. Differences in parasitic losses from device to device only further complicate the issue.

Power output from harvester devices can vary wildly with the type of input excitation, and the excitations to which devices are subjected for experimental characterization differ significantly from one device to another. No standardized battery of benchtop input excitations yet exists in the literature that can allow for a proper comparison of device performance, and power output using uncontrolled inputs—such as that of arm swing during locomotion or shaking a device by hand—varies significantly from test to test even for the same device under testing, and thus cannot be used as a reliable indicator of relative device performance without a substantial population of test subjects operating under controlled conditions.

Finally, the dynamic response of the mechanical substructure of a vibration energy harvester is heavily influenced by the values of the characteristic parameters that define its design. For example, the power output of a linear resonant vibration energy harvester subjected to harmonic forcing is highly dependent on a choice of spring constant that allows for resonance with the input. How does one compare the relative merit of two dissimilar devices if one is carefully optimized for maximum power output and the other is not?

The purpose of this work is to attempt to create conditions under which a comparison of a subset of popular device architectures is as valid as possible. To this end, six simple device architectures have been selected on the basis of research interest in the literature, and a comparative analysis of these architectures under arm swing excitations has been performed to examine the relative merit of each architecture in wrist-worn energy harvesting applications.

In this work, it is not assumed that the harvester electromechanical coupling is small; thus, the backwards coupling of the transducer and its consequent effects on the mechanical dynamics cannot be ignored. Often, a linear viscous damper is employed to model the effects that the transducer has on the mechanical harvester dynamics, and the dissipative effect of this damper—herein referred to as *electrical damping*—provides a simple way to compute harvester power output; this will be the approach used for the comparative analysis presented here. By treating the energy dissipation effects that the transducer has on the mechanical dynamics in this way, the mechanical architecture may be studied as effectively 'decoupled', or independent from, the electrical domain, facilitating a comparison of mechanical architectures.

Fixing the transducer type to that which is mathematically described by a linear viscous damper may not be as restrictive a practice as it may initially appear. Firstly, a linear viscous damper can indeed represent an optimal transducer force capable of maximizing harvester power output in response to certain excitations [19, 20]. However, it would be unwise to assume the optimality of linear viscous damper transducer dynamics for all—or even most—architectures and all excitations [21–24].

More important is the observation that the effects that both piezoelectric and electromagnetic transducers have on the mechanical harvester dynamics can be effectively captured by the addition of linear damping and a shift in the harvester oscillation frequency even for nonlinear harvester architectures—at least in the case of Duffing-type oscillators [25, 26].

Because a linear viscous damper serves as a good model for low-frequency electromagnetic energy harvesting as a result of direct application of Faraday's law of induction to a purely resistive lumped element electrical domain model [27], the most narrow interpretation of this work would be limited in application to only low-frequency electromagnetic energy harvesting. However, if the observations made in [26] are permitted to extend to other nonlinear systems, such as those described in this paper, then the method used for this comparative analysis has the potential to apply to harvesters with electromagnetic, piezoelectric, and hybrid electromagnetic-piezoelectric transducers under other excitation scenarios.

2. Device architectures

Motivated by previous research efforts and commercial endeavors (see section 1), six simple device architectures are proposed for the purpose of comparative analysis: one rotational architecture, and two linear architectures, as well as counterparts with linear spring elements. Frictional losses are modeled as linear viscous in nature, with a damping coefficient b_m. As described in section 1, electrical transduction is also assumed to be linear viscous in nature, acting in parallel with the mechanical damping, with an electrical damping coefficient b_e. The total viscous damping coefficient is $b = b_m + b_e$. A discussion on the individual architectures and their mathematical models now follows.

2.1. Rotational structures

The first structure considered in the analysis, herein denoted as the *rotor, unsprung rotor,* or *unsprung rotational* structure or architecture, is comprised of an eccentric seismic mass that rotates about an axis, as in [3]. The second structure, herein denoted as the *sprung rotor* or *sprung rotational* structure or architecture, is identical to the rotor structure, except that a torsional spring acts on the mass, with a spring constant that typically causes the rotor to rest in the upper (with respect to gravity) semicircle in the absence of external input. See figure 1.

A derivation of the rotor architecture model now follows for the convenience of the reader, as well as to correct a minor error in a similar model derivation found in [3] and used in [28]. This derivation also differs from that found in [6] in its generality; instead of considering individual forcing cases, generalized forcing from arbitrary combinations of linear accelerations and rotations in the z direction (refer to figure 1) are considered. See table 1 for variable definitions.

Because the Lagrangian approach will be used to derive the equation of motion, the derivation for the rotational structure begins by considering multiple coordinate frames useful for computing the total system energy; O_0 is an inertial

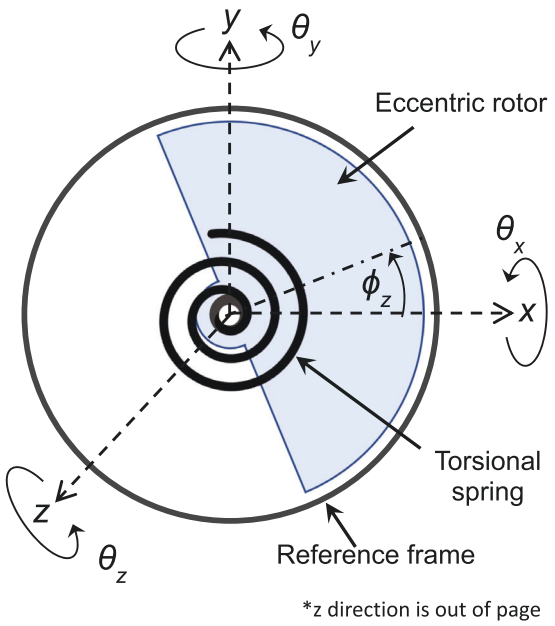

Figure 1. Illustration of the sprung rotor harvester architecture.

Table 1. Variable definitions for rotational model derivation.

Variable	Definition
m	Mass of rotor
I_g	Moment of inertia of rotor about center of gravity
b	Linear viscous damping coefficient for rotational damper
k	Linear spring constant for torsional spring
ψ	Angle of centerline of rotor as measured from basis vector $\boldsymbol{x}_0$
θ	Angle of basis vector $\boldsymbol{x}_1$ as measured from basis vector $\boldsymbol{x}_0$ ('housing angle')
ϕ	Angle of basis vector $\boldsymbol{x}_2$ as measured from basis vector $\boldsymbol{x}_1$ ('relative rotor angle')
X	Scalar displacement of O_1 in basis vector $\boldsymbol{x}_0$ direction ('absolute housing displacement')
Y	Scalar displacement of O_1 in basis vector $\boldsymbol{y}_0$ direction ('absolute housing displacement')
x'	Scalar displacement of O_2 in basis vector $\boldsymbol{x}_1$ direction
y'	Scalar displacement of O_2 in basis vector $\boldsymbol{y}_1$ direction
$\boldsymbol{p}$	Displacement vector from O_2 to center of gravity (Eccentric length, $\|\boldsymbol{p}\| = L$)
$\boldsymbol{d}_{01}$	Inter-origin vector from O_0 to O_1
d_{12}	Inter-origin vector from O_1 to O_2
${}^0R_1$	Rotation matrix from coordinate frame O_1 to O_0
${}^1R_2$	Rotation matrix from coordinate frame O_2 to O_1

reference frame, O_1 is a reference frame fixed to the rotor housing, and O_2 is a reference frame fixed to the rotating rotor mass. See figure 2. It is assumed that out-of-plane rotations contribute a negligible amount of kinetic energy to the rotor mass, and are thus ignored in the model derivation.

This derivation considers the combined effects of coordinate frame acceleration and gravity as a single effective

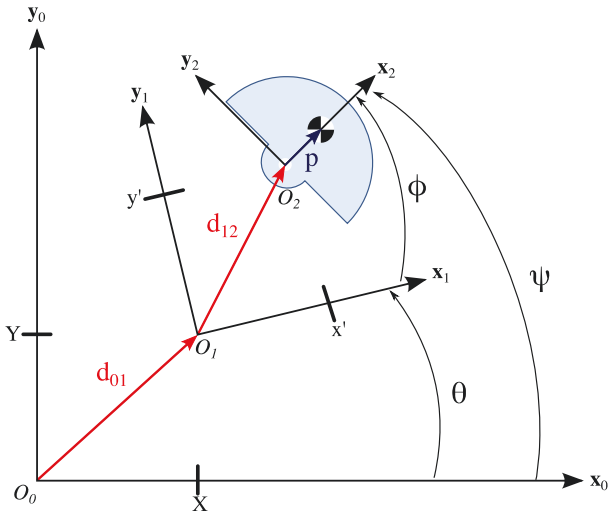

Figure 2. Schematic of rotational harvester structure used for the derivation of the equation of motion.

acceleration; the reason for this is that accelerometers typically report net acceleration—that is, total acceleration of O_1 from motion plus effective acceleration from gravity—and this approach enables the use of direct accelerometer readings as model input. Therefore, acceleration input values $\ddot{x}$ and $\ddot{y}$ (to be introduced later) are really the combination of linear acceleration and gravity, as would be reported by an accelerometer. Thus, the potential energy contribution from gravity will be ignored without any loss of model generality, making $U = 0$ in the Lagrangian.

Kinetic energy is considered at the center of mass of the rotor, and is composed of translational and rotational components:

$$T = \frac{1}{2}m\,\|\boldsymbol{v}\|^2 + \frac{1}{2}I_g\dot{\psi}^2.$$

First, locate the point ${}^2\boldsymbol{p} = \begin{bmatrix} L \\ 0 \end{bmatrix}$ in O_0. Express the displacement vector as

$$\begin{aligned} {}^0\boldsymbol{r} &= {}^0\boldsymbol{d}_{01} + {}^0R_1{}^1\boldsymbol{d}_{12} + {}^0R_1{}^1R_2{}^2\boldsymbol{p} \\ &= \begin{bmatrix} X + x'\cos\theta - y'\sin\theta + L\cos(\theta+\phi) \\ Y + x'\sin\theta + y'\cos\theta + L\sin(\theta+\phi) \end{bmatrix}. \end{aligned}$$

So far, no constraints have been placed on x' and y' (the displacements of O_2 as measured from O_1). This was done for generality. Now assume $x' = y' = 0 = \text{constant}$, which corresponds to the axis of rotation coinciding with coordinate frame of O_1 for all time. With this assumption, differentiation of ${}^0\boldsymbol{r}$ with respect to time yields

$$\frac{\mathrm{d}}{\mathrm{d}t}{}^0\boldsymbol{r} = \boldsymbol{v} = \begin{bmatrix} \dot{X} - L\dot{\psi}\sin\psi \\ \dot{Y} + L\dot{\psi}\cos\psi \end{bmatrix}.$$

Since $\psi = \theta + \phi$, substitution of $\boldsymbol{v}$ into the expression for kinetic energy yields

$$T = \frac{1}{2}m[(\dot{X} - L\dot{\psi}\sin\psi)^2 + (\dot{Y} + L\dot{\psi}\cos\psi)^2] + \frac{1}{2}I_g\dot{\psi}^2.$$

The Lagrangian is formed by $\mathcal{L} = T - U = T$ and the Euler–Lagrange equation is invoked to find the stationarity condition, in conjunction with the Rayleigh dissipation function $R = \frac{1}{2}b(\dot{\psi} - \dot{\theta})^2$ to account for the effect of damping between O_1 and the rotor mass, to obtain the equation of motion for the rotor:

$$\ddot{\psi} = -\frac{mL(\ddot{Y}\cos\psi - \ddot{X}\sin\psi) + b(\dot{\psi} - \dot{\theta})}{mL^2 + I_g}.$$

Typically, accelerometers report acceleration values expressed in terms of a coordinate system fixed to the accelerometer. Thus, the time-varying functions $\ddot{X}(t)$ and $\ddot{Y}(t)$ (the scalar components of the vector representing the acceleration of O_1 expressed in the O_0 coordinate frame) are not useful inputs in practice. Because this acceleration is merely a vector $\boldsymbol{a} \in \mathbb{R}^2$ expressed in O_0, make use of the coordinate frame transformation to re-express this vector in O_1, denoted ${}^1\boldsymbol{a}$:

$${}^1\boldsymbol{a} = {}^0R_1{}^{\mathrm{T}}\begin{bmatrix}\ddot{X}\\ \ddot{Y}\end{bmatrix} = \begin{bmatrix}\cos\theta & \sin\theta\\ -\sin\theta & \cos\theta\end{bmatrix}\begin{bmatrix}\ddot{X}\\ \ddot{Y}\end{bmatrix}.$$

Make the substitutions $\ddot{X} = \ddot{x}\cos\theta - \ddot{y}\sin\theta$ and $\ddot{Y} = \ddot{x}\sin\theta + \ddot{y}\cos\theta$ then simplify:

$$\ddot{\psi} = -\frac{mL(\ddot{y}\cos(\psi - \theta) - \ddot{x}\sin(\psi - \theta)) + b(\dot{\psi} - \dot{\theta})}{mL^2 + I_g}. \tag{1}$$

Finally, note that one is often not concerned with the angle of the rotor with respect to an inertial frame; the relative angle is typically more important. Substituting $\psi = \theta + \phi$ yields

$$\ddot{\phi} = -\frac{mL(\ddot{y}\cos\phi - \ddot{x}\sin\phi) + b\dot{\phi}}{mL^2 + I_g} - \ddot{\theta} \tag{2}$$

so that the equation of motion may be solved for $\phi(t)$ directly.

The addition of a torsional spring simply adds a restoring torque to the rotational mass that is proportional to the relative angle, ϕ. The zero-torque angle is taken to be $\phi = \pi/2$ by convention. Thus, the sprung rotor architecture is described by

$$\ddot{\phi} = -\frac{mL(\ddot{y}\cos\phi - \ddot{x}\sin\phi) + b\dot{\phi} + k\left(\phi - \frac{\pi}{2}\right)}{mL^2 + I_g} - \ddot{\theta} \tag{3}$$

Note that the unsprung rotor model (2) corresponds to a special case of (3) where $k = 0$.

Average power output of a rotational device under a particular excitation signal of length T is found by solving the relevant equation of motion and numerically integrating the instantaneous power dissipated in the electrical damper over the length of the signal; that is, $P_{\mathrm{avg}} = \frac{1}{T}\int_0^T b_e\dot{\theta}^2\mathrm{d}t$.

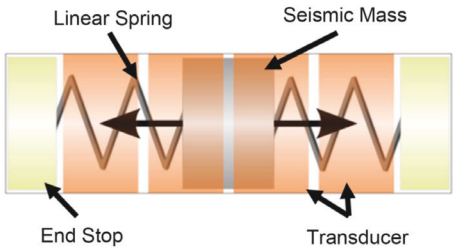

Figure 3. One-dimensional sprung linear slide architecture.

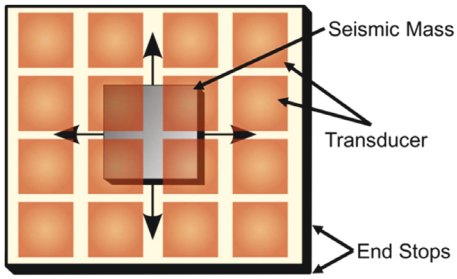

Figure 4. Two-dimensional linear slide structure.

2.2. Linear structures

Four of the six structures in the analysis are comprised of a single seismic mass free to translate within a plane with one or two degrees of freedom. The first of these four structures considered is the *one-dimensional linear slide*, comprised of a seismic mass that is free to move in a single dimension up to the length of the device, wherein impact occurs. The *one-dimensional sprung linear slide* structure or architecture is simply the one-dimensional linear slide with a restoring force provided by a spring. See figure 3. Additionally, two-dimensional analogs of the one-dimensional linear slide architectures were considered that are composed of pairs of linear damper and spring elements acting orthogonally and independently on the single seismic mass within the two available degrees of freedom. These structures are denoted as either the *two-dimensional linear slide* structure (see figure 4) or the *two-dimensional sprung linear slide* structure, depending on the presence of spring elements.

In the case of the one-dimensional slide structures, it is assumed that accelerations orthogonal to the direction of the degree of freedom have negligible impact on the dynamics and are thus ignored; the only acceleration considered in the model is that which acts along the direction in which the seismic mass may move. Additionally, the effects of rotation of the slide housing—and the resulting centrifugal forces—are also considered negligible and are ignored in the derivation. As a consequence of these simplifying assumptions, the equation of motion for the one-dimensional sprung slide may be described by the classical

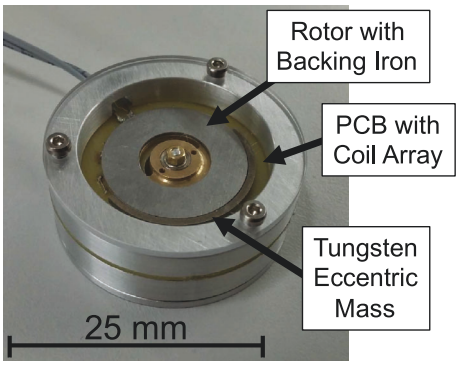

Figure 5. Sprung (and unsprung) rotational prototype device with electromagnetic transducer.

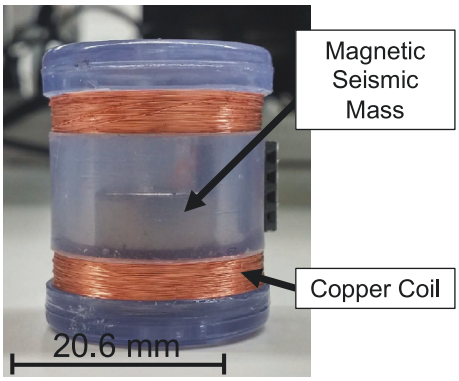

Figure 6. One-dimensional unsprung linear slide prototype device with electromagnetic transducer.

base excitation equation

$$m\ddot{z} + b\dot{z} + kz = -\ddot{a}, \tag{4}$$

where z is the displacement of the seismic mass relative to the housing, m is the seismic mass, b is the total linear viscous damping coefficient, k is the spring constant, and $\ddot{a}$ is the linear acceleration of the housing in the direction of the single degree of freedom, as in [29]. The unsprung one-dimensional slide is also modeled by (4) in the special case that $k = 0$.

It is important to note that (4) describes the motion of the seismic mass only at points where it does not make contact with the end stops. When contact occurs, it is assumed that this reaction to the end stop may be described as an impact that reverses the velocity of the seismic mass before impact, v_A, and modifies it by the coefficient of restitution $0 \leqslant e \leqslant 1$, i.e. velocity after impact $v_B = -ev_A$.

In order to model the two-dimensional slide structures, (4) is applied independently in each direction of motion using independent values of k and b in each direction.

Finally, average power output of a linear device under a particular excitation signal of length T is found by solving the relevant equation of motion and numerically integrating the instantaneous power dissipated in the electrical damper over the length of the signal; that is, $P_{\text{avg}} = \frac{1}{T}\int_0^T b_e \dot{z}^2 \mathrm{d}t$.

3. Model validation

In order to corroborate the harvester architecture models developed in section 2, prototype devices were constructed and their performance quantified under various excitations.

To validate the rotational harvester models, a rotational prototype device was fabricated. An electromagnetic transducer was selected for ease of construction and for desirable transducer physics; that is, the transducer torque is approximately proportional to angular velocity. The prototype can be unsprung, or house a torsional spring. See figure 5.

Similarly, a simple one-dimensional linear slide prototype device was fabricated. Again, an electromagnetic transducer was selected. See figure 6.

The workflow for corroborating all of the models involves first characterizing the device in order to determine the various coefficient values to be used in the model—spring constants, damping coefficients, mass, etc. Then, the prototype is subjected to either a known vibrational input and the voltage output waveform across a resistive load is recorded, or is subjected to an uncontrolled input and both the output waveform and inertial data are simultaneously recorded using an inertial measurement unit (IMU). Power dissipation in a resistive load is computed. The values of the coefficients characterizing the prototype device, along with the necessary vibrational input, is fed into the corresponding model, and the dissipated power from the model is compared with the dissipated power computed from empirically measuring output voltage waveforms.

3.1. Device characterization

In order to make use of the models developed in section 2, values for the various coefficients were determined for the prototype under consideration.

For the rotational prototypes, mass, inertia and center of mass location were determined using SolidWorks Computer Aided Design software's Mass Properties tool. The values for mass estimated from this tool were checked against empirical mass measurements of individual prototype components to help ensure reasonable accuracy of the other estimated parameters. Values for torsional spring constants were estimated by observing the frequency of free oscillation of the rotor mass and recording the response with a high-speed camera. See figure 7. Values for mechanical and electrical viscous damping coefficients were also found by recording the free oscillation of the rotor mass with a high-speed camera and applying the log decrement method to the response decay envelope. This process was repeated for all spring constants used in the sprung rotor device prototype, as well as the unsprung rotor prototype which was allowed to oscillate under the effect of gravity. Finally, the obtained values for b_m and b_e for the sprung and unsprung prototypes were averaged to map the list of damping values to single-valued coefficients to be used for all simulations.

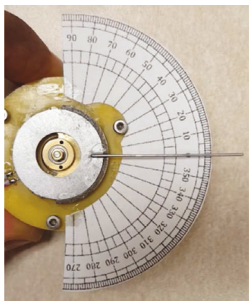

Figure 7. Experimental setup for estimating viscous damping coefficients.

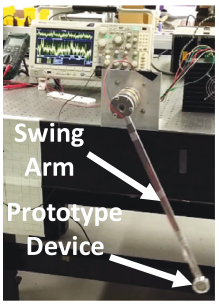

Figure 8. Swing arm experimental setup during operation.

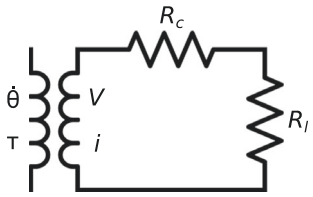

Figure 9. Lumped element model of harvester electrical domain showing power conjugate variables. Notice that coil inductance is neglected.

Figure 10. Example voltage waveform across load resistor generated by unsprung rotational prototype under pseudo-walking excitation.

For the linear slide prototype, the seismic mass (a cylindrical magnet) was measured with a scale. The coefficient of restitution was estimated by dropping the mass from a known height in an elongated version of the prototype and observing the height after collision with an end stop. Mechanical damping was estimated by inclining an elongated version of the prototype at a known angle with respect to gravity and recording the time taken by the seismic mass to traverse the length of the prototype; with all other coefficients known, the damping coefficient can then be backed out of (4). The electrical damping of the linear prototype was far more difficult to measure primarily because of the small range of displacements (the distance between coils) over which significant electrical damping is applied to the seismic mass. Thus, the approach for estimating this parameter involved solving for the magnetic field of the magnet using finite element software and performing numerical surface integration to estimate flux through the coils over a range of magnet displacements. The rate of change of flux with respect to displacement could then be computed and, after assuming a load resistance matched with the measured coil resistance, the electrical damping coefficient could be computed.

3.2. Swing arm test setup

A controlled input excitation can aid in the understanding of the dynamical behavior of harvester architectures, as well as provide a reasonable means for a performance comparison of prototype devices. To this end, a *swing arm* benchtop empirical testbed was developed, which is composed of a computer-controlled stepper motor driving a 0.5 m long aluminum pendulum. Prototype devices are mounted on the distal end of the swing arm and are driven using a sinusoidal excitation with a fixed swing frequency and swing angle amplitude; an input signal hereafter referred to as *pseudo-walking* input. See figure 8. A coil-resistance-matched resistive load is installed across the output terminals of the prototype under consideration in order to provide a means of power dissipation. Voltage waveforms across the resistive load are recorded using a data acquisition system. Because the stepper motor and the motor controller generate a considerable amount of electromagnetic interference in the prototype electromagnetic transducers, a low pass filter with a cutoff frequency of 10 Hz is used to filter the voltage waveforms. The voltage waveforms are then stored and exported for processing after each experimental run.

To compute average power dissipation in the load resistances, the root mean square (rms) voltage across the resistive load, V_{rms}, is computed at each sampled point, and the instantaneous power at each sampled point found using $P_{\text{inst}} = V_{\text{rms}}^2/R_l$. Average power dissipation in the load resistance is determined by taking the mean of the regularly sampled instantaneous power values P_{inst} over the entire signal. See figure 9. An example of a load voltage waveform across coil-resistance-matched resistive load produced by the unsprung rotational prototype under pseudo-walking excitation is shown in figure 10.

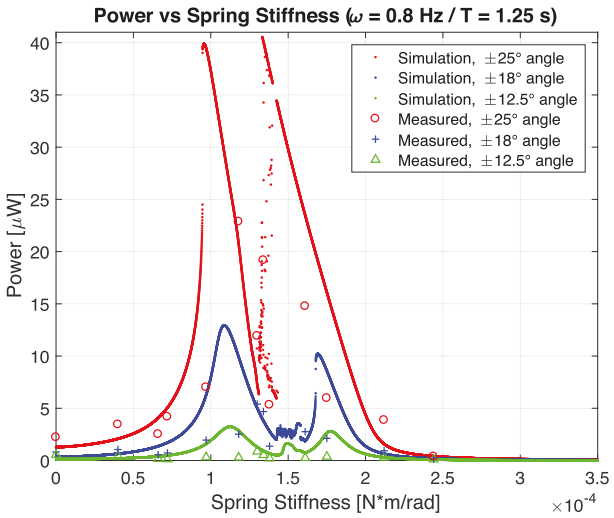

Figure 11. Average power versus torsional spring stiffness plot for pseudo-walking swing arm frequency of 0.8 Hz (1.25 s period) at multiple excitation amplitudes.

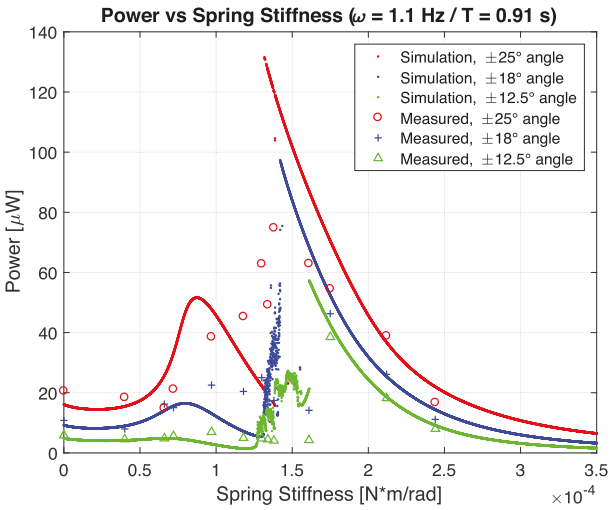

Figure 13. Average power versus torsional spring stiffness plot for pseudo-walking swing arm frequency of 1.1 Hz (0.91 s period) at multiple excitation amplitudes.

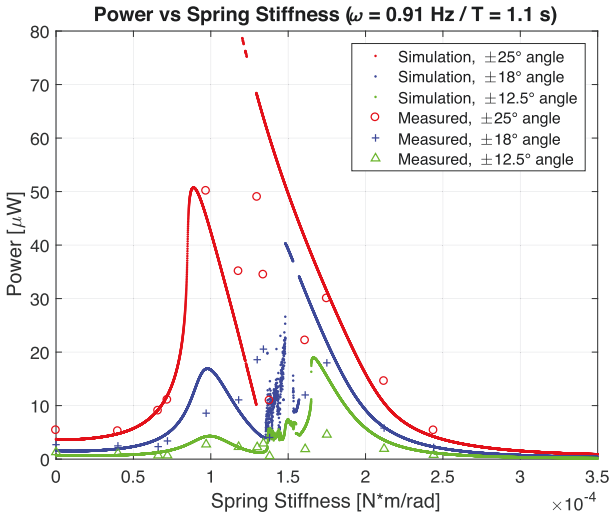

Figure 12. Average power versus torsional spring stiffness plot for pseudo-walking swing arm frequency of 0.91 Hz (1.1 s period) at multiple excitation amplitudes.

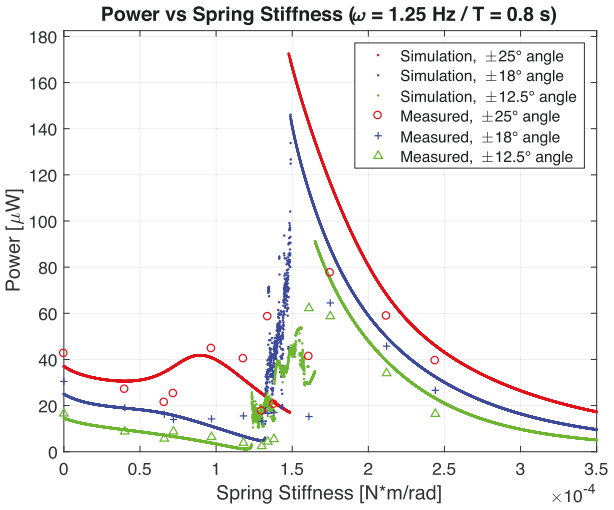

Figure 14. Average power versus torsional spring stiffness plot for pseudo-walking swing arm frequency of 1.25 Hz (0.8 s period) at multiple excitation amplitudes.

3.3. Rotational structure swing arm results

The stiffness of the torsional spring plays a major role in the dynamic response of the sprung rotor, and thus has the potential to greatly impact power output. Considering the importance of this parameter on device performance, a natural choice in evaluating the predictive power of the mathematical models is examining how well empirical measurement of average device power fits a simulated average power versus spring stiffness plot under swing arm excitation. A coil-resistance-matched resistive load of $R_l = 240\,\Omega$ was installed across the output terminals to provide a means for power dissipation and measurement. See figures 11–14, and note that the performance of an unsprung rotor device corresponds to zero spring stiffness in the plots.

In order to produce the plots found in figures 11–14, 10 000 regularly spaced spring constant values ranging from $k = 0$ N m rad^{-1} (unsprung) to $k = 3.5 \times 10^{-4}$ N m rad^{-1} were fed into the sprung rotor model, along with the relevant device parameters, and various types of swing arm excitation. The length of simulation was 90 s. The average power calculation did not begin until 60 s into each simulation to reduce the effect that initial conditions may have on average output power. Due to the presence of a matched load resistance, it was assumed that half of the power reported by the model was lost to the coil resistance. Consequently, a factor of ½ was applied to the average power value reported by the model.

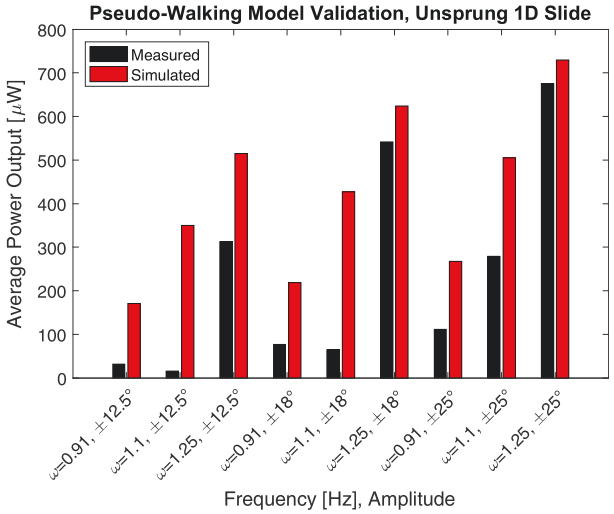

Figure 15. Measured versus simulated power output of the unsprung linear slide prototype subject to pseudo-walking excitation.

Note that the impedance due to coil inductance at the low frequencies used in this analysis is negligible.

Figures 11–14 indicate generally good agreement between simulation and empirical measurement over most spring constants. However, experimentally validating the sharp peak in power output at specific spring stiffness values was particularly challenging as only a finite number of spring stiffness values could be tested, and a measurement of the spring stiffness could not be performed with accuracy until after the spring was installed in the prototype device. Initial conditions may also play a significant role in the long-term behavior of the rotational architectures that can make empirical corroboration of the peaks difficult; see section 4.3 for further discussion.

3.4. Linear structure swing arm results

Being that the linear model proposed in section 2.2 has been corroborated under a variety of circumstances in the literature, only a simplified model validation procedure was carried out for the unsprung one-dimensional slide prototype pictured in figure 6 for the sake of completeness. The battery of pseudo-walking signals used to validate the sprung and unsprung rotational models (see sections 3.2 and 3.3) was employed to validate the unsprung linear model. A coil-resistance-matched resistive load of $R_l = 420\,\Omega$ was installed across the output terminals of the linear prototype in order to provide a means of power dissipation and measurement. A factor of ½ was applied to the average power value reported by the model, as in section 3.3. The experimental results are plotted in figure 15.

It is clear from figure 15 that the behavior of the prototype device is not captured particularly well by the model presented in section 2.2. However, there are several important points to note: firstly, the prototype was not designed to exhibit friction that is linear viscous in nature (nor was the prototype fabricated with low-friction materials; note the relatively high value for mechanical damping in table 2). It is quite possible that, at low excitation frequencies and amplitudes, coulombic friction effects—especially that of static friction—dominate the behavior, and these effects are not captured when the damping is modeled using a linear viscous damper. The increase in simulation accuracy seen in figure 15 as swing arm frequency or amplitude are increased appears to support this claim. Secondly, the electrical damping coefficient was not measured in as direct a manner as the mechanical damping coefficient for the linear prototype, as explained in section 3.1. Considering the relatively crude means by which this parameter was estimated, it is perhaps unsurprising that the simulation does not better fit the measured data over all tested excitations.

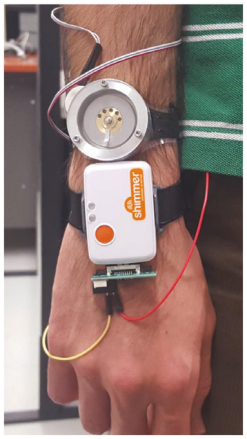

Figure 16. One of two prototype device and Shimmer3 pairs mounted on the right wrist of a participant before a human subject test.

3.5. Rotational structure human subject results

In order to further corroborate the rotational model developed in section 2, a comparison between empirically measured average power dissipation across a resistive load and simulated power dissipation under real walking excitation was desired. To accomplish this, 10 human subjects were tasked with walking on a treadmill at 3.5 mph (approximately $1.56\,\mathrm{m\,s^{-1}}$), a fast-paced walk. Two rotational prototypes were affixed together to either the left or right wrist; one unsprung prototype, and one sprung prototype with a spring constant $k = 1.05 \times 10^{-4}\ \mathrm{N\,m\,rad^{-1}}$, which simulations suggest is near optimal for this type of excitation and the level of damping present in the prototype. Once again, a coil-resistance-matched resistive load of $R_l = 240\,\Omega$ was installed across the output terminals of each rotational prototype in order to provide a means of power dissipation and measurement. Two Shimmer3 data acquisition units [30] independently sampled the output voltage waveforms across the load resistances of each prototype device while simultaneously recording IMU data at a sampling frequency of approximately 51 Hz during the walking activity. See figure 16. The small amount of data recorded before and after the walking activity were discarded for the power calculations and simulation

Table 2. Measured prototype parameters for use in model validation.

Rotational prototypes		Linear prototypes	
Parameter	Value(s)	Parameter	Value(s)
Rotating mass, m	10.7 g	Seismic mass, m	17.2 g
Inertia about center of gravity, I_g	819 g·mm^2	Coefficient of restitution, e	0.1
Eccentric length, L	1.52 mm	End stop distance, d	7.14 mm
Torsional spring constant, k	0–3.5 $\times$ 10^{-4} N m rad^{-1}	Linear spring constant, k	0
Mechanical damping, b_m	5.94 $\times$ 10^{-7} N m rad^{-1} s^{-1}	Mechanical damping, b_m	9.3 $\times$ 10^{-2} N m^{-1} s^{-1}
Electrical damping, b_e	1.87 $\times$ 10^{-6} N m rad^{-1} s^{-1}	Electrical damping, b_e	0.222 N m^{-1} s^{-1}

input. Average power dissipation in the load resistance was computed exactly as described in section 3.2.

To simulate average power dissipation in the prototype devices, the IMU data collected with the Shimmer3 device were fed into the mathematical models along with the relevant measured prototype parameters. The first 5 s of the simulation data were ignored in the average power calculation to reduce the effect that initial conditions have on power output. Again, it was assumed that half of the power reported by the model was lost to the coil resistance. Consequently, a factor of ½ was applied to the average power value reported by the model.

Figure 17 shows the correspondence between measured power output and predicted power output from the unsprung rotor prototype and model. Although the simulated power output mostly tracks the broad trends between subjects, there exists significant disagreement between empirically measured and simulated average power output for several individual subjects. The source of this disagreement is not clear, and such disagreement does not persist in simulations of the sprung rotational model, as will be discussed next.

Figure 18 shows the correspondence between measured power output and predicted power output from the sprung rotor prototype and model. The agreement between measurement and simulation is generally very good, even when making the comparison for most individual subjects. Binning the error in simulated power output for both the sprung and unsprung rotational models makes it clear that the model makes more accurate predictions for the sprung device in general, and the model is significantly less accurate in predicting power output for the unsprung device. See figure 19.

Sources of error in both the sprung and unsprung rotational device models include: inaccuracy in the measurement of prototype device parameters, finite IMU acceleration and rotation rate resolution, and inaccuracies in IMU data that are a consequence of the fact that the IMU cannot occupy the exact same location on the arm as the prototype device during testing, and thus collects inertial data that do not exactly reflect the real accelerations and rotations experienced by the prototype during testing.

Causes for the disparity in error between the sprung and unsprung rotor models, as summarized in figure 19, are less forthcoming, but could be a result of numerical instability in the governing differential equation for the unsprung rotational model that does not appear to be exhibited by its sprung counterpart, or even sensitivity to initial conditions exhibited by the unsprung rotational model under real walking data excitation. A study on the role that initial conditions play on the long-term power output for sprung and unsprung devices under human subject excitation is beyond the scope of this work. For a brief discussion on the effect of initial conditions on the rotational model under a particular pseudo-walking excitation, see section 4.3.

4. Comparative analysis

With the mathematical models experimentally validated and qualified, the next step in the analysis is to compare the relative performance of the different device architectures discussed in section 2 via simulation. Device volumes (defined as the volume swept by the seismic mass displaced through the configuration space of its center of mass) were first fixed to an arbitrary 1 cm^3 for the simulations. Tungsten seismic masses (density $\rho = 19\,000$ kg m^{-3}) were assumed for each device architecture. Mechanical damping coefficients were fixed. Two distinct input vibration types—pseudo-walking and data collected from real walking input—were considered in the comparison. Characteristic design parameters for each architecture model were optimized for each input signal in order to maximize average power output for that signal. Average power output was compared between device architectures, as well as power output sensitivity and variation in in optimal parameters.

4.1. Mechanical damping

The rotational viscous damping coefficient was fixed at an arbitrary $b_{m1} = 1 \times 10^{-7}$ N m rad^{-1} s^{-1}—a choice motivated by experience with achievable levels of viscous damping for rotational devices on the scale considered in the analysis. In order to derive a comparable damping coefficient for the linear structures, a cyclical energy balance was considered: given an arbitrary periodic relative rotor motion $\phi(t)$ with an associated value of work $W_{b_{m1}}$ over the period of motion, find a value of the linear viscous damping coefficient that, if a linear viscous damper applied a damping force proportional to the velocity of a particle positioned at the center of mass of the rotor undergoing the periodic motion $\phi(t)$, the damper attached to the particle would dissipate (do) an equivalent

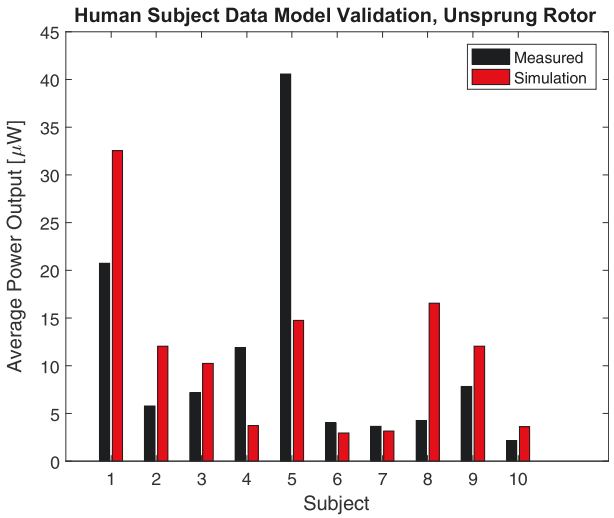

Figure 17. Measured versus simulated power output for the unsprung rotor prototype subject to real walking data.

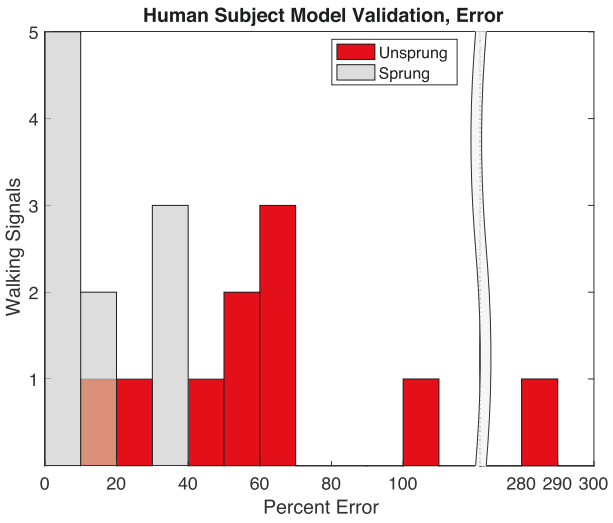

Figure 19. Histogram of error in power output for rotor models subject to real walking data.

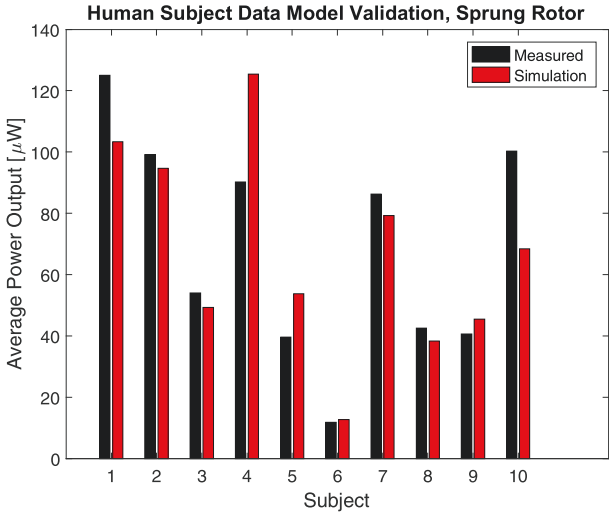

Figure 18. Measured versus simulated power output for the sprung rotor prototype subject to real walking data.

value of work, $W_{b_{m2}}$. That is,

$$W_{bm1} = W_{bm2}$$

$$\oint b_{m1}\dot{\phi}\mathrm{d}\phi = \oint b_{m2}\dot{x}\mathrm{d}x,$$

$$b_{m1}\oint \dot{\phi}^2\mathrm{d}t = b_{m2}L^2\oint \dot{\phi}^2\mathrm{d}t$$

such that $b_{m2} = b_{m1}/L^2$. Using the eccentric length of a 2 mm thick rotational device $L = 5.4$ mm, the associated linear viscous damping coefficient is $b_{m2} = 0.0034$ kg s, which was the value used for the linear devices in the comparative analysis.

4.2. Optimization

The specific set of values of an architecture's design parameters, such as electrical damping or torsional spring constant, greatly impact the nature of the dynamic response of a given architecture to excitation, and thus the performance of the architecture in terms of average power output. Consequentially, for a fair comparison of architectures, it is desirable to first find the optimal set of values for each architecture that maximize average power output in response to a particular input excitation. Then, with device volumes fixed and dissipative losses reasonably equated (see section 4.1), average power output becomes a sensible metric for gauging relative performance.

However, input signals considered in this work include those obtained from human subjects during walking that are quite complex in nature and, in the case of the rotational structures, the differential equations describing the harvester architecture are highly nonlinear. As a consequence, the relationship between design parameters, input excitation, and average power output is not known until the equations of motion describing the harvester have been numerically solved and average power output computed. In order to set up an optimization problem, an objective function was formed, which took in design parameters and input excitation data as arguments, numerically solved the relevant differential equation using zero initial conditions for the state variables and, ignoring the first portion of the solution in an attempt to reduce the effect of initial conditions, returned the average output power of the harvester. Objective functions formed using the output of numerical ordinary differential equations solvers are nonsmooth—a consequence of solution variation within the bounds of user-defined error tolerance—and many local minima appear on the objective function surface. Worse yet, larger scale local minima may also be present as a result of the problem being nonconvex, in general. Furthermore, objective function evaluations are computationally costly, as the input signals may be fairly long (40 s or more), making brute-force optimization approaches impractical. For problems involving the optimization of parameters of ordinary differential equations, such as the one described above,

Table 3. Examples of the types of optimization problems (in nonstandard form) solved for each input signal for the comparative analysis. Electrical damping b_e, spring constant k, and geometry parameters α, w, l, L serve as optimization variables, P_{avg} is the objective function that returns average power output, and x_{lb} and x_{ub} indicate lower and upper x-variable bounds, respectively.

Sprung rotational harvester		Sprung linear harvester	
maximize $_{b_e,k}$	$P_{\text{avg}}(b_e, k, \alpha)$	maximize $_{b_e,k,w,l,L}$	$P_{\text{avg}}(b_e, k, w, l, L)$
subject to	$b_{\text{lb}} \leqslant b_m \leqslant b_{\text{ub}}$	subject to	$b_{\text{lb}} \leqslant b_e \leqslant b_{\text{ub}} \quad l - L \geqslant 0$
	$0 \leqslant k \leqslant k_{\text{ub}}$		$0 \leqslant k \leqslant k_{\text{ub}} \quad lwt = V$
	$\alpha_{\text{lb}} \leqslant \alpha \leqslant \alpha_{\text{ub}}$		$d_{\text{lb}} \leqslant w, l, L \leqslant d_{\text{ub}}$

MATLAB's Pattern Search (PS) algorithm is a good solver choice [31].

In order to attempt to search through multiple basins of attraction in the search space, but allow for efficient convergence to the minimum within a promising basin of attraction, a hybrid optimization scheme was used: a genetic algorithm (GA) was used for a global search of the solution space that passed the best solution to the PS algorithm for convergence to a minimum—a routine similar to that recommended in [32]. Relatively large population sizes and elevated mutation rates were used to search the solution space with the GA, and tight mesh tolerances on the PS algorithm (in addition to tightened solution tolerances of the numerical solver) assisted in achieving consistent optimization results for a given input signal.

In addition to optimizing electrical damping coefficients and spring constants, geometric parameters were exposed as optimization variables in order to determine the geometric configuration of the architectures that maximize power output. Device thickness is a major consideration for a wrist-worn device, and this design variable will almost certainly be heavily constrained in any real application. As a result, three arbitrary thicknesses of 2, 3, and 4 mm were selected for the devices, which were fixed during the optimization procedure. In this way, unreasonably thick or thin optimization solutions were precluded from consideration, and the dimension of the solution space could be reduced by one variable. This approach also serves to make comparisons between different structures easier. If device thickness is fixed, the only remaining geometric variable for the rotational geometry is the sector angle of the rotor. For the one-dimensional linear slide structures, the total device length, the seismic mass length, and the seismic mass width are the remaining variables that define the geometry; for the two-dimensional slide structures, seismic mass length and device length in the additional dimension are also necessary to fully define the geometry.

The value for the coefficient of restitution, e, in the linear slide architectures was found to have no practical impact on device performance and was thus excluded as a design variable to be optimized. This unexpected result is a consequence of the optimization procedure itself; the optimal electrical damping for the linear models was found to be that which avoided contact with the end stops, which reduces power output. Related consequences of end stop contact are discussed in section 4.6.

Finally, in order to improve the quality and reliability of the optimization output as well as preclude impossible designs, practical bounds were placed on some of the design variables. For example, an arbitrary device length of $d_{\text{ub}} = 3$ cm was chosen to be a practical limiting case for a wrist-worn device, and a maximum rotor sector angle of $\alpha_{\text{ub}} = 2\pi$ was chosen to prevent the optimization algorithms from searching over impossible sector angles. See table 3 for examples of optimization problems that were solved in this work.

4.3. Effect of initial conditions

Being that the architectures presented in section 2 are nonlinear dynamical systems, it is reasonable to be concerned about the degree to which initial conditions may play a role in determining the long-term behavior (and, by extension, power output) of such systems under various excitations. A numerical approach was taken in an attempt to partially address this concern for the rotational architectures; 1000 regularly spaced spring constant values ranging from $k = 0$ N m rad^{-1} (unsprung) to $k = 3 \times 10^{-4}$ N m rad^{-1} were fed into the sprung rotor model, along with the relevant device parameters, to produce a plot similar to that of (the highest amplitude excitation found in) figure 13. However, for each spring constant, many ($65^2 = 4225$) initial conditions (ICs) were given to the model instead of just the zero initial condition. The ICs were evenly dispersed in a region of the phase space considered to be within nominal operating conditions for the harvester: initial angles of $-\pi/2 \leqslant \phi \leqslant \pi/2$ rad and initial angular velocities of $-6\pi \leqslant \dot{\phi} \leqslant 6\pi$ rad s^{-1}, including the origin. The simulation output is captured in the plot found in figure 20.

The plot in figure 20 suggests that there are multiple distinct orbits that persist long after the start of the simulation that produce disparate values of power. However, most of the harvester orbits described in the plot that correspond to various nonzero ICs coincide with the points that correspond to the zero initial condition, including some of the highest power orbits. This suggests that, although initial conditions do indeed play a role in the steady state dynamics of the sprung rotational architecture for certain spring stiffness values, this role does not serve to advantage the rotational architecture unfairly when zero initial conditions are assumed in the optimization procedure described in section 4.2. Furthermore, the existence of multiple steady state power values seen in figure 20 provides a plausible explanation for the

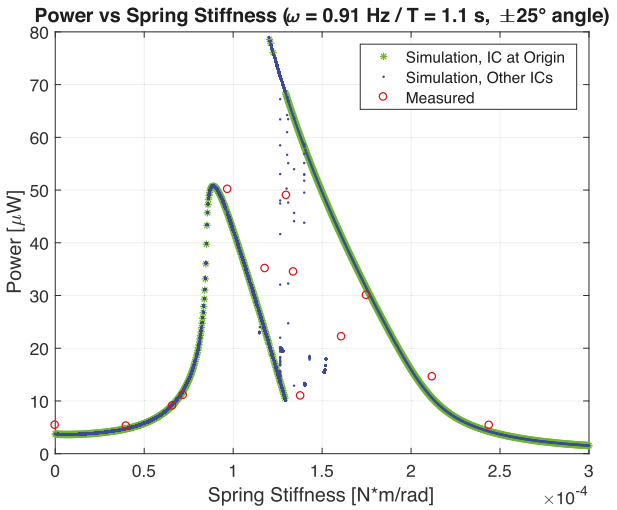

Figure 20. Power versus spring stiffness for multiple ICs. Note that for some values of spring stiffness, there are multiple stable periodic orbits that produce different mean power values.

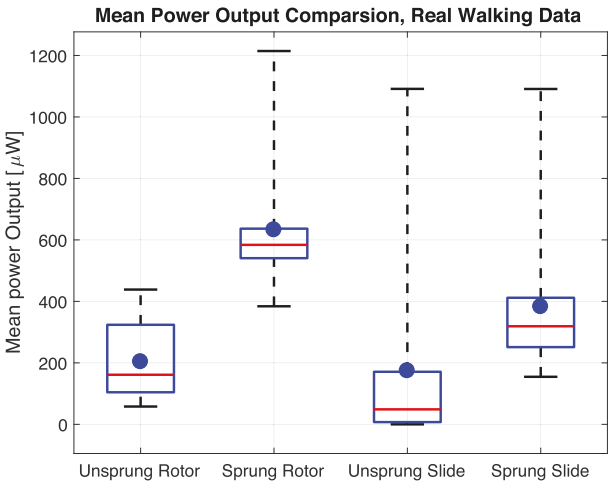

Figure 21. Box plot indicating the median, maximum, and minimum average power output for each device, along with quartiles. Mean average power output is indicated with a blue circle.

disagreement between simulation and experimental measurement seen for mid-range values of spring stiffness in figures 11–14.

The simulation-based analysis described in this section is by no means exhaustive. Generating the plot found in figure 20 is very computationally expensive, and further analysis focusing on the dynamics of the rotational system is required to better understand the nuances of this behavior—this is beyond the scope of this work.

4.4. Pseudo-walking

The first optimization routines were applied to the linear and rotational device models described in section 2 under a synthesized pseudo-walking input (see section 3.2) with a swing period of 1.1 s ($\omega \approx 0.91$) and a swing arm amplitude of $\pm 18°$. The computer-generated signals were 40 s in length, and the first 10 s of the harvester response were ignored in the calculation of average power to reduce the effect that initial conditions may have on the average output power. The primary results of the optimization can be found in table 4.

The results of the optimization across device thickness in table 4 are unsurprising; with device volumes held constant, the rotational structures benefit from an increased distance from the rotating center to the center of mass of the rotor, increasing the lever arm on which linear forces act. Thus, under the pseudo-walking signal, table 4 suggests that a thinner rotational device outperforms a thicker rotational device. The same scaling relationships are not shared among the linear devices, which is also unsurprising; if the thickness of a linear structure is constrained, the same seismic mass can be achieved by increasing the width of the device.

In all cases, sprung and unsprung, rotational and linear, the optimal design variables for geometry converged to the same point: the seismic mass consuming ½ of the total device volume. For rotational devices, this suggests that the optimal sector angle is 180° and, for linear devices where the width of the seismic mass is the same as the device width, this suggests that the seismic mass should be ½ the total device length.

Missing from table 4 are the optimized power output results from the two-dimensional linear slide device architectures; this is because these architectures consistently converge upon the optimal one-dimensional linear slide architecture parameters during optimization, suggesting that the additional degree of freedom does not result in increased harvester performance over the analogous one-dimensional architectures. For this reason, the two-dimensional linear slide architectures were omitted from further analysis after this stage of optimization.

It is clear from table 4 that the addition of a spring can greatly increase the mean output power of rotational devices under pseudo-walking input; for a 2 mm device thickness, the increase in mean power is approximately 851%. For linear devices, however, no increase in mean power output is observed at all. Notice that for a 2 mm device thickness, the one-dimensional linear slide architectures outperform the sprung rotational architecture by 21% under pseudo-walking excitation. It is important to note that the mean linear acceleration of the pseudo-walking signal along the direction of the single degree of freedom of the one-dimensional linear slide architecture is zero; this fact has implications on device performance that are discussed in section 4.6.

4.5. Real walking data

The real walking data collected from the wrists of 10 human subjects during a controlled 3.5 mph walking experiment (see section 3.5) were used as input to the rotational and linear device models described in section 2 to allow for a comparison of structures under real walking excitations. The optimization scheme described in section 4.2 was applied to each architecture for every individual input, so that the maximum average power output for all architectures was determined for every subject. However, it should be noted that the results presented in section 4.3 suggest that the

Table 4. Mean power output under pseudo-walking input for optimized structures with varying device thicknesses.

Thickness	Unsprung rotor mean power	Sprung rotor mean power	Unsprung 1D slide mean power	Sprung 1D slide mean power
2 mm	38.8 μW	369 μW	448 μW	448 μW
3 mm	30.5 μW	295 μW	448 μW	448 μW
4 mm	25.8 μW	253 μW	448 μW	448 μW

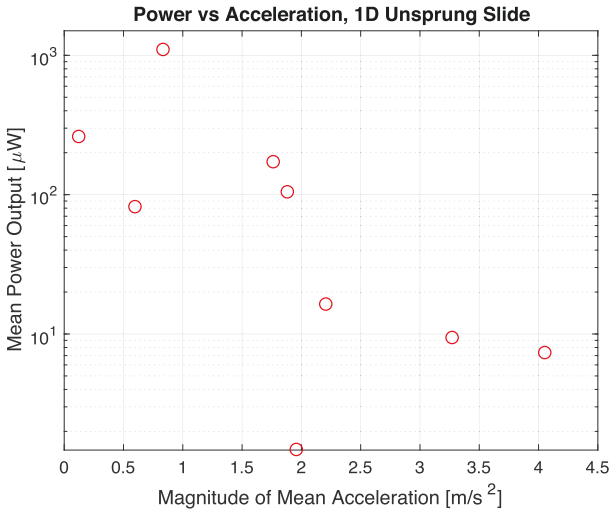

Figure 22. Semi-log plot of average power dissipation versus mean walking signal acceleration magnitude for the optimized unsprung slide.

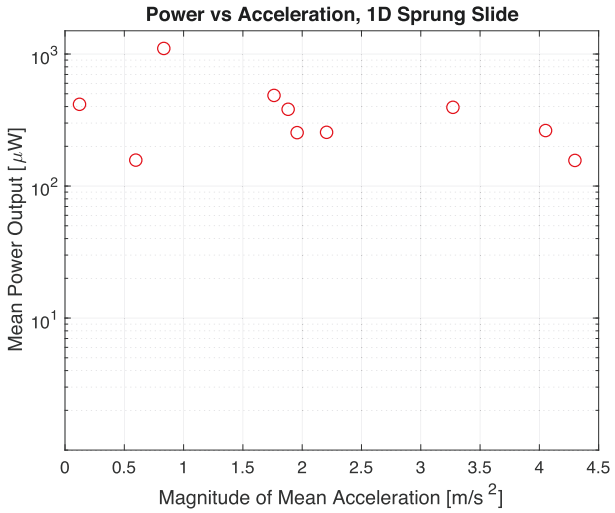

Figure 23. Semi-log plot of average power dissipation versus mean walking signal acceleration magnitude for the optimized sprung slide.

optimal geometric configuration of all harvesters ensures that the seismic mass consumes ½ of the total device volume. Running the optimization routine using other pseudo-walking signals or real walking data not discussed in this analysis suggest that this configuration is optimal regardless of the input excitation. Thus, in order to reduce the dimension of the solution space, all geometric parameters were fixed to this presumed optimal geometric configuration. The results of this study are presented in figure 21.

The results summarized in figure 21 indicate that the addition of a spring to rotational structures improves mean power output by an average of 211% under real walking excitation. For the linear structures, the addition of a spring improves power output by an average of 120% under real walking excitation. Finally, the sprung rotational architecture outperforms the sprung linear architecture by approximately 66% on average under real walking excitation.

A more thorough discussion regarding the performance of the one-dimensional slide structures can be found in section 4.6.

4.6. Power variation of the one-dimensional linear slide

The variation in power output for the one-dimensional unsprung linear slide under real walking excitation is very large relative to the other structures, as can be seen in figure 21. The trajectories of the seismic mass under these excitations appear to indicate that, if a significant *acceleration bias* exists in the input signal—that is, a nonzero mean acceleration over the length of the signal—the seismic mass tends to come to rest against the end stops of the device for a significant portion of the input signal. As a consequence, the average power output decreases. The presence of this acceleration bias in real walking signals may be explained by a tendency for the arm to swing about a nonzero angle with respect to gravitational acceleration, unlike a simple pendulum [33, 34], resulting in a nonzero net acceleration acting on the mass over the length of the signal. Such an inverse relationship between power output and acceleration bias appears to be demonstrated in figure 22, whereby the average power output of the optimized one-dimensional unsprung linear slide is plotted against the magnitude of the mean acceleration of the signal. A similar plot for the optimized one-dimensional sprung linear slide is given in figure 23. The magnitude (absolute value) was specifically considered because the orientation of the x-axis of the Shimmer3 device changes depending on whether the right or left wrist of the subject was used for the walking experiment described in section 3.5.

As the magnitude of the acceleration bias increases, the seismic mass is more likely to rest against an end stop for a significant duration of the signal, thereby reducing mean power output. Operating under this assumption, it is reasonable to assume that the addition of a spring, and thus a restoring force that tends to move the mass towards the center of the slide, should reduce the effect that the acceleration bias has on power output, as the restoring force tends to keep the

Table 5. Comparison of power output when architectures are individually optimized for each signal and power output when a single compromise solution is employed for the design parameters.

	Unsprung rotor	Sprung rotor	Unsprung 1D slide	Sprung 1D slide
Mean power, individual optimization	204 μW	636 μW	174 μW	383 μW
Mean power, compromise	168 μW	513 μW	138 μW	276 μW
Power reduction	18%	19%	21%	28%

mass away from the end stops. Figure 23 appears to support this claim, as the relationship between the magnitude of the acceleration bias and mean power output is far less pronounced for the sprung linear slide than it is for the unsprung linear slide.

The results presented in table 4 become more understandable when operating under this acceleration bias hypothesis; the acceleration bias of all pseudo-walking signals is zero, as the driven pendulum on which the pseudo-walking signal is based oscillates about an angle that is collinear with respect to gravitational acceleration. The linear slide structures operate with great efficacy under these conditions, producing greater power output when compared to the rotational structures under this excitation. With no restoring force necessary to compensate for nonzero acceleration bias, the spring constant of the sprung linear slide architecture approaches zero during optimization, and the power output of the sprung and unsprung slide structures converge.

Finally, the acceleration bias hypothesis may also explain why the two-dimensional linear slide structure converges to the one-dimensional analog during optimization under pseudo-walking excitation, as mentioned in section 4.3: the acceleration bias in the additional direction of motion is approximately that of Earth's gravitational acceleration, which is large relative to the orthogonal direction of motion. If it is indeed the case that it is difficult for the linear slide structures to generate power under a large acceleration bias, then it is not surprising that the optimized geometric configuration of the two-dimensional slide is to maximize displacements in a direction perpendicular to that of gravity. Thus, the optimal two-dimensional slide becomes a one-dimensional slide.

4.7. Variation in optimal parameters

Thus far, the power output of each device under consideration in the comparative analysis has been accomplished by using the set of device parameters that optimizes power output for each input signal. Fortunately, it appears that a single set of geometric parameters is optimal for all architectures under any input excitation (see section 4.3). However, this is not the case for the remaining design parameters: the electrical damping coefficient and (when applicable) spring stiffness, which vary considerably from input to input in order to achieve optimality. If the use of passive components is desired (a static transducer architecture producing a single effective electrical damping coefficient, for example, or a spring of a single stiffness value), then the characteristic harvester parameters cannot change in response to the type of input excitation. As a result, the set of parameters that are optimal for one type of input signal could be significantly suboptimal for another, and harvester power output will not be maximized over both inputs.

A *compromise solution* that generates reasonably high power output over a range of input excitations using a single, unchanging set of harvester parameters is desired. One approach to obtain such a solution is to simply average the values of the optimization solutions obtained for a set of signals of interest. For this exercise, the human subject data described in section 3.5 is used as the set of input signals over which a compromise solution will be determined. The average power output of each architecture is found first by individually optimizing each architecture to maximize power output for each of the ten walking signals and averaging the results; this is identical to the procedure described in section 4.5 yielding the average power results presented in figure 21. Then, the optimal design parameters found via optimization for each architecture are averaged, producing a single set of design parameters for each architecture. Using these parameters, the average power output over the ten walking signals is again computed for each architecture. The results of this procedure are summarized in table 5.

The results presented in table 5 make it clear that not only do the rotational architectures outperform the linear architectures under real walking excitation when each parameter is optimized from signal to signal as described in section 4.5, but the rotational architectures also suffer less performance degradation when a single set of averaged design parameters is used for all walking signals. Coincidentally, the sprung rotational architecture with averaged optimal design parameters again produced an average of 66% more mean power output than the sprung linear architecture with averaged optimal design parameters.

5. Conclusions

A simulation-based comparative analysis of six vibration energy harvesting architectures was performed. This was accomplished by first deriving device models, then validating these models by virtue of experiment. An optimization procedure was employed to find the values of the device design parameters that maximized average power output under synthesized pseudo-walking input and real walking data collected from 10 human subjects during a controlled walking experiment.

For the rotational architectures, the addition of a spring greatly improved power output. Under a pseudo-walking input, average power output for the sprung structure was

851% higher than that of the unsprung structure. Under real walking input, the addition of a spring improved mean power output over the 10 walking signals by an average of approximately 211%. It is important to point out that this improvement comes at the cost of structural asymmetry, as the zero-torque position of the sprung rotational seismic mass must be in the upper half of the device volume with respect to gravity in order to realize the power improvement.

For the linear architectures, the addition of a spring gave mixed results. Under pseudo-walking excitation, optimal spring stiffness values approached zero for the sprung devices, indicating that the addition of a spring does not provide an opportunity for enhanced power output; the performance of the sprung and unsprung architectures are identical under this type of excitation. However, using real walking data as input, the addition of a spring increased mean device power output by an average of approximately 120% over the 10 walking signals, while also reducing the variance in power output between individual walking signals. The two-dimensional linear architectures were only considered in the pseudo-walking portion of the comparative analysis, as the optimal geometry was found to be identical to that of the analogous one-dimensional structures, suggesting that the additional degree of freedom does not provide a pathway for increased power output.

The sprung architectures, rotational or linear, represented the device structures capable of producing the greatest power output in the study. Under pseudo-walking excitation, both sprung and unsprung linear architectures produced 21% more mean power than the sprung rotational architecture. However, under real waking excitation, the sprung rotational architecture outperformed the sprung linear slide architecture by 66% when optimal parameters were used for each walking signal.

Finally, an averaged optimal solution was employed for all architectures to investigate the performance impact that passive components with static parameter values would have on harvester power output. Even under these circumstances, the sprung rotational architecture outperforms the sprung one-dimensional architecture by 66%.

The limited scope of the comparative analysis represents its primary limitation. A small, albeit common, subset of device architectures was examined, and nonlinear device components, such as softening or hardening springs, were excluded from the analysis. Only a limited set of excitations were used in the study, primarily to limit computational effort in searching for optimal device parameters, but also to narrow the input signals to those which appear representative of typical wrist-worn harvester excitations during human locomotion. The effect that initial conditions has on the long-term behavior of the architectures in the study was only superficially explored in the rotational architectures and, although the brief analysis suggested that the effect is minimal, assuming zero initial conditions for all architectures remains a potential shortcoming of the study. Finally, in an effort to focus on the mechanical harvester substructures, many interesting and potentially exploitable areas of research, such as active circuit manipulation techniques, were ignored.

Acknowledgments

Funding for this research was provided by the National Science Foundation under Award Number ECCS 1342070, and a generous grant from Analog Devices Inc.

ORCID iDs

R Rantz https://orcid.org/0000-0002-5805-4170
M A Halim https://orcid.org/0000-0003-3879-9017
T Xue https://orcid.org/0000-0002-3235-7536

References

[1] Nakano J, Komori K, Hattori Y and Suzuki Y 2015 MEMS rotational electret energy harvester for human motion *J. Phys.: Conf. Ser.* **660** 12052
[2] Romero E, Neuman M R and Warrington R O 2011 Rotational energy harvester for body motion *2011 IEEE 24th Int. Conf. Micro Electro Mech. Syst.* pp 1325–8
[3] Xue T, Ma X, Rahn C and Roundy S 2014 Analysis of upper bound power output for a wrist-worn rotational energy harvester from real-world measured inputs *J. Phys.: Conf. Ser.* **557** 012090
[4] Xue T and Roundy S 2017 Sensors and actuators a: physical on magnetic plucking configurations for frequency up-converting mechanical energy harvesters *Sensors Actuators* A **253** 101–11
[5] Boland J, Chao Y-H C Y-H, Suzuki Y and Tai Y C 2003 Micro electret power generator *6th Annu. Int. Conf. Micro Electro Mech. Syst. 2003, MEMS-03 (Kyoto)* (Piscataway, NJ: IEEE) pp 538–41
[6] Yeatman E M 2008 Energy harvesting from motion using rotating and gyroscopic proof masses *Proc. Inst. Mech. Eng.* C **222** 27–36
[7] Lockhart R, Janphuang P, Briand D and de Rooij N F 2014 A wearable system of micromachined piezoelectric cantilevers coupled to a rotational oscillating mass for on-body energy harvesting *2014 IEEE 27th Int. Conf. Micro Electro Mech. Syst.* pp 370–3
[8] Pillatsch P, Yeatman E M and Holmes A S 2014 A piezoelectric frequency up-converting energy harvester with rotating proof mass for human body applications *Sensors Actuators* A **206** 178–85
[9] Pillatsch P, Yeatman E M and Holmes A S 2013 Real world testing of a piezoelectric rotational energy harvester for human motion *J. Phys.: Conf. Ser.* **476** 12010
[10] Kinetron 2014 Micro Generator System '26.4' www.kinetron.eu
[11] Hayakawa M 1991 Electronic wristwatch with generator US5001685 A
[12] Tang Q C, Yang Y L and Li X 2011 Bi-stable frequency up-conversion piezoelectric energy harvester driven by non-contact magnetic repulsion *Smart Mater. Struct.* **20** 125011
[13] Naruse Y, Matsubara N, Mabuchi K, Izumi M and Suzuki S 2009 Electrostatic micro power generation from low-frequency vibration such as human motion *J. Micromech. Microeng.* **19** 94002
[14] Elvin N G and Elvin A A 2011 An experimentally validated electromagnetic energy harvester *J. Sound Vib.* **330** 2314–24
[15] Halim M A and Park J Y 2014 A non-resonant, frequency up-converted electromagnetic energy harvester from human-body-induced vibration for hand-held smart system applications *J. Appl. Phys.* **115** 094901

[16] Renaud M, Fiorini P, van Schaijk R and van Hoof C 2009 Harvesting energy from the motion of human limbs: the design and analysis of an impact-based piezoelectric generator *Smart Mater. Struct.* **18** 35001
[17] Bowers B J and Arnold D P 2009 Spherical, rolling magnet generators for passive energy harvesting from human motion *J. Micromech. Microeng.* **19** 94008
[18] Kiziroglou M E, He C, Yeatman E M and Member S 2009 Rolling rod electrostatic microgenerator *IEEE Trans. Ind. Electron. Control Instrum.* **56** 1101–8
[19] Halvorsen E, Le C P, Mitcheson P D and Yeatman E M 2013 Architecture-independent power bound for vibration energy harvesters *J. Phys.: Conf. Ser.* **476** 117–21
[20] Heit J and Roundy S 2015 A framework to find the upper bound on power output as a function of input vibration parameters *Energy Harvest. Syst.* **1** 69–78
[21] Hosseinloo A H and Turitsyn K 2014 Fundamental limits to nonlinear energy harvesting *Phys. Rev. Appl.* **4** 064009
[22] Hosseinloo A H, Vu T L and Turitsyn K 2015 Optimal control strategies for efficient energy harvesting from ambient vibrations *Proc. 54th Ann. Conf. on Decis. Control* pp 5391–6
[23] Le T T, Truong B D, Le C P and Sager S 2016 On the power optimization of the vibration-based energy harvesters under swept input acceleration *Proc. IEEE Sensors 2016* pp 1–3
[24] Truong B D, Le C P and Halvorsen E 2015 Experiments on power optimization for displacement-constrained operation of a vibration energy harvester *J. Phys.: Conf. Ser.* **660** 1–5
[25] Daqaq M F, Masana R, Erturk A and Dane Quinn D 2014 On the role of nonlinearities in vibratory energy harvesting: a critical review and discussion *Appl. Mech. Rev.* **66** 40801
[26] Karami M A and Inman D J 2011 Equivalent damping and frequency change for linear and nonlinear hybrid vibrational energy harvesting systems *J. Sound Vib.* **330** 5583–97
[27] Mitcheson P, Green T C, Yeatman E M and Holmes A S 2004 Architectures for vibration driven micropower generators *J. Microelectromechanic Syst.* **13** 429–40
[28] Rantz R, Xue T, Zhang Q, Gu L, Yang K and Roundy S 2016 Comparative analysis of wrist-worn energy harvesting architectures *J. Phys.: Conf. Ser.* **773** 012076
[29] Inman D J 2014 *Engineering Vibration* 4th edn (London: Pearson)
[30] Realtime Technologies Ltd 2016 'Shimmer User Manual Revision 3m', http://shimmersensing.com/images/uploads/docs/Shimmer_User_Manual_rev3n.pdf, (Accessed: 01-January-2017)
[31] Mathworks 2016 'Global Optimization Toolbox: User's Guide (R2016b)', http://mathworks.com/help/pdf_doc/gads/gads_tb.pdf, (Accessed: 15-September-2016)
[32] Wetter M and Wright J 2003 Comparison of a generalized pattern search and a genetic algorithm optimization method *8th Int. IBPSA Conf.* pp 1401–8
[33] Gutnik B, MacKie H, Hudson G and Standen C 2005 How close to a pendulum is human upper limb movement during walking? *HOMO- J. Comput. Hum. Biol.* **56** 35–49
[34] Kuhtz-Buschbeck J P, Brockmann K, Gilster R, Koch A and Stolze H 2008 Asymmetry of arm-swing not related to handedness *Gait Posture* **27** 447–54